Population Growth Dynamics of Carbon Nanotubes

Mostafa Bedewy, Eric R. Meshot, Michael J. Reinker, and A. John Hart*

Mechanosynthesis Group, Department of Mechanical Engineering, University of Michigan, 2350 Hayward Street, Ann Arbor, Michigan 48109, United States

ABSTRACT

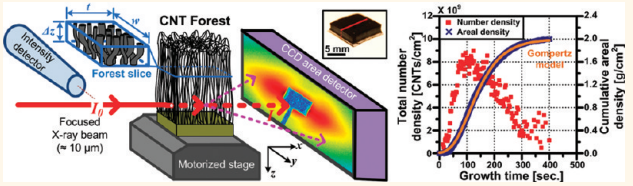

Understanding the population growth behavior of filamentary nanostructures, such as carbon nanotubes (CNTs), is hampered by the lack of characterization techniques capable of probing statistical variations with high spatial resolution. We present a comprehensive methodology for studying the population growth dynamics of vertically aligned CNT forests, utilizing high-resolution spatial mapping of synchrotron X-ray scattering and attenuation, along with real-time height kinetics. We map the CNT alignment and dimensions within CNT forests, revealing broadening and focusing of size distributions during different stages of the process. Then, we calculate the number density and mass density of the CNT population *versus* time, which are true measures of the reaction kinetics. We find that the mass-based kinetics of a CNT population is accurately represented by the S-shaped Gompertz model of population growth, although the forest height and CNT length kinetics are essentially linear. Competition between catalyst activation and deactivation govern the rapid initial acceleration and slow decay of the CNT number density. The maximum CNT density (*i.e.*, the overall catalyst activity) is limited by gas-phase reactions and catalyst-surface interactions, which collectively exhibit autocatalytic behavior. Thus, we propose a comprehensive picture of CNT population growth which combines both chemical and mechanical cooperation. Our findings are relevant to both bulk and substrate-based CNT synthesis methods and provide general insights into the self-assembly and collective growth of filamentary nanostructures.

KEYWORDS: carbon nanotubes · kinetics · filaments · X-ray · characterization · population · chemical vapor deposition · catalyst

Engineering of materials comprising highly ordered nanostructures requires an understanding of the collective behavior of individual nanostructures in a large population. While many destructive and nondestructive techniques can be employed for measuring the geometry and dimensions of individual nanostructures, there are fewer methods capable of interrogating large populations thereof. The importance of acquiring and understanding statistical information arises from the fact that a macroscopic assembly of nanostructures typically consists of an extremely large number of individual nanoscale elements. For instance, a 1 cm^2 substrate area of an array of vertically aligned carbon nanotubes (CNTs), a so-called "forest", typically contains more CNTs than there are humans on earth. In this and many other examples, there is a profound gap between measurements of individual nanostructures and measurements of the bulk properties of materials. This gap spans the challenge of obtaining representative statistics on the size and/or the distribution of nanostructures throughout a physical space, which limits essential insights into the causes of variation in the final material properties. Advances in population-based analysis of nanostructures will also be necessary for use of statistical methods to analyze and control the quality of nanostructured materials and their production, much like is commonplace in traditional manufacturing operations.

CNT forests are a model system for investigating the population dynamics of nanostructure synthesis and are an attractive material design that potentially enables the utilization of the properties of billions of CNTs in parallel. Importantly, it has recently come to light that typical CNT forests have a complicated and spatially non-uniform morphology, including gradients (*e.g.*, from top to bottom) of alignment, diameter, and packing density.[1−6] These variations depend on the multivariate conditions used for CVD growth. Nevertheless, many investigations of CNT forest properties have assumed a perfectly uniform morphology reflecting point-wise or average characteristics of the CNTs (diameter, density). In many cases, such ideal morphology is needed to optimize functional properties; hence, a more detailed understanding of the morphology is needed to accurately model mechanical, thermal, electrical, and other properties that depend on hierarchical network effects.[7−9]

* Address correspondence to ajohnh@umich.edu.

Received for review August 16, 2011 and accepted October 23, 2011.

Published online October 23, 2011
10.1021/nn203144f

Highly uniform ensembles of monodisperse CNTs are needed for electrical interconnects,[10−12] filters,[13] gas sensors,[14−16] and structural composites.[17] Also, consistent morphology is required for post-synthesis processing such as the spinning of CNTs from forests into yarns and sheets,[18,19] which was shown to depend on the CNT areal density and bundle organization within a forest.[20]

An accurate picture of the internal structure of CNT forests is also essential for understanding how to control the growth process to approach the ideal structure. In fact, the kinetic picture of how a population of CNTs evolves with time during synthesis is still largely incomplete. The CNTs within a forest nucleate from a population of catalyst nanoparticles having a distribution of sizes and shapes, whose morphology was shown to evolve during growth,[4,21] resulting in a distribution of CNT sizes, and likely a polydispersity of growth rates. On the basis of our recent observation that the number and mass density of CNTs change during growth and considerably decay (by almost an order of magnitude) toward termination,[1] the apparent forest height kinetics measured *in situ*[22−28] or *ex situ*[29−31] must be complemented by a measure of the mass kinetics. The discrepancy between forest height kinetics and mass kinetics further explains the abruptness of forest growth self-termination,[1] which we[25] and others[27,32−36] have observed.

Several *in situ* and *ex situ* methods for nondestructively measuring CNT forest height have been developed, such as optical photography and videography,[24,27] optical interference,[22] single-slit laser diffractography,[37] time-resolved reflectivity,[23] and cycling of growth conditions to form marks that are visible in electron microscopy.[30,31,38] Methods of accurate and nondestructive mass measurements are fewer and generally use a microbalance either *in situ*[39] or *ex situ*,[1,40] which is limited by the resolution of the balance and cannot be used for spatial mapping. Alternatively, the changes in contrast from *ex situ* Z-contrast transmission electron microscopy (Z-STEM) images, as well as changes in the estimated effective extinction coefficient from time-resolved optical reflectivity (TRR), were used to infer information about CNT forest density.[41] Although these methods can be used for spatial profiling, they can only provide relative measures of density and cannot give absolute density values.

In addition, *in situ* Raman spectroscopy has been used to infer CNT growth kinetics from real-time monitoring of the area under the G-band.[42−45] Because the CNT−laser coupling strength depends on the structure, diameter, and number of walls of a CNT, it is unlikely that the G-band intensity is directly proportional to the total mass of a polydisperse CNT population.[46] For both single-wall (SWNT) and multiwall (MWNTs) CNTs, the line shape of the G-band is a superposition of multiple peaks which depend on the CNT chirality, conductivity, and charge transfer with the surroundings.[46,47] Further, for a typical millimeter-sized CNT forest, Raman spectroscopy cannot be reliably used to get population measurements because the laser beam cannot fully penetrate the forest. The presence of non-CNT graphitic deposits can also contribute to the G-band intensity. Hence, Raman studies require either a single CNT or a relatively limited number thereof to give relative mass measurements and require small diameter SWNTs to give structural information about size and chirality.

We previously showed how small-angle X-ray scattering (SAXS)[48,49] and ultra-small-angle X-ray scattering (USAXS)[50] can provide precise measurements of the diameter, bundle size, and alignment of CNTs within a forest. Here we present a comprehensive nondestructive characterization methodology for CNT materials, which enables identification of the population kinetics of the CNT growth process. This method combines high-resolution spatially resolved X-ray scattering and intensity attenuation measurements after growth, with real-time measurements of CNT forest height during growth. The spatial and temporal evolution of the mass density, number density, and cumulative CNT areal density are analyzed with unprecedented accuracy from the initial CNT self-organization stage until growth termination. On the basis of these findings, we can explain growth of a CNT forest as a time-varying population. This population behavior results from a statistical ensemble of individual particles and CNTs having polydisperse reaction behavior, contrasting previous studies that explained CNT forest growth kinetics based on models for a single particles and/or CNTs.[23,32,51,52] Population growth models indicate that CNT synthesis exhibits an autocatalytic and cooperative nature, and that the maximum density of CNTs is limited by the process conditions. Finally, surface analysis of the catalyst gives insights into how competition between catalytic activation and deactivation rates prevent indefinite growth of CNTs using current CVD methods.

RESULTS AND DISCUSSION

Our methodology for CNT population analysis begins with high-resolution spatial mapping of the forest using synchrotron X-ray scattering. We place an already-grown CNT forest (Figure S1 in Supporting Information) on a motorized stage in the beampath of a synchrotron X-ray beam that is focused using monocapillary optics, as shown in Figure 1A. By scanning the forest from top to bottom at increments of 10 μm, which is approximately equal to the beam size, we discretize the forest into a stack of differential volumes that we refer to as "slices". Two different types of data are acquired for each slice: (1) X-ray scattering patterns, collected using a 2D area detector; and (2) X-ray intensity, collected using detectors placed upstream and downstream of the CNT forest. We also measure

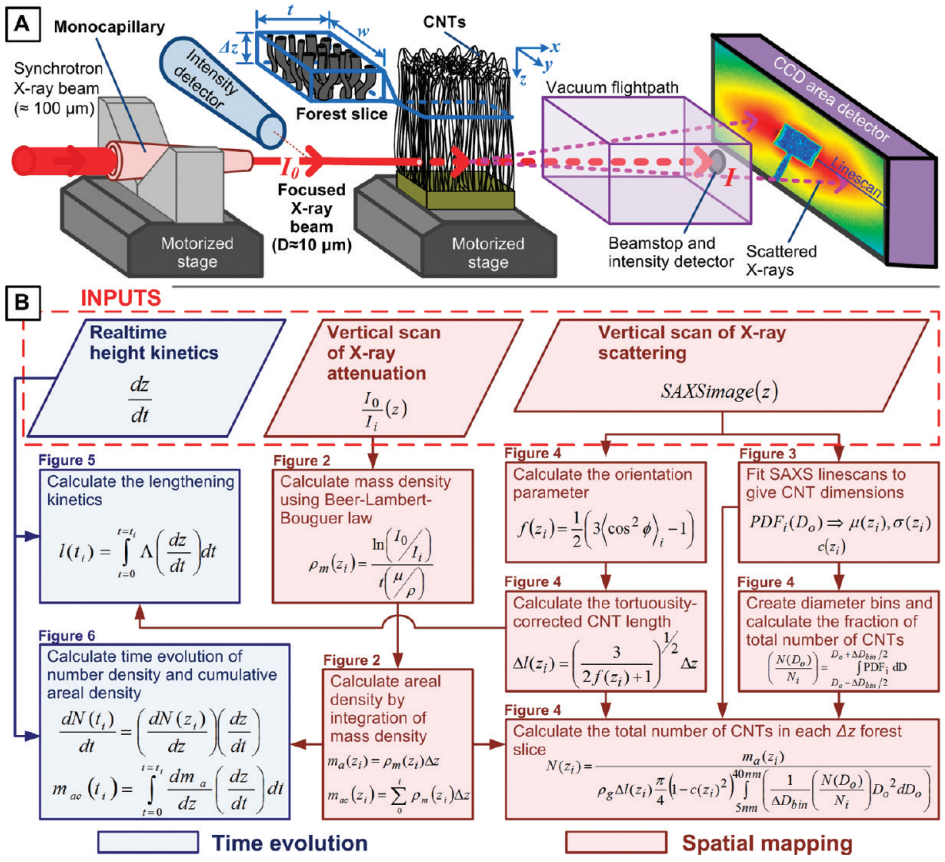

Figure 1. Method of X-ray mapping and analysis of CNT populations: (A) schematic of experimental setup for simultaneous spatially resolved synchrotron X-ray mass attenuation and scattering measurements; (B) quantitative analysis procedure incorporating real-time CNT height measurements with X-ray data to give mass and number density kinetics. The figure labels above each box indicate where the respective results are shown.

the CNT forest height *versus* time *in situ* during growth (see Methods section). Both the *in situ* and *ex situ* data are inputs to the quantitative analysis procedure shown in Figure 1B.

First, we use the measurements of X-ray intensity to calculate the local mass density of the CNT forest within the beampath, according to the Beer–Lambert–Bouguer law.[53,54] This relates the density of a material to the X-ray intensity attenuation due to both scattering and absorption, such that

$$\rho_m(z_i) = \frac{\ln\left(\frac{I_0}{I_i}\right)}{t\left(\frac{\mu}{\rho}\right)} \quad (1)$$

Here $\rho_m(z_i)$ is the local mass density obtained from each forest slice (index i), defined as the mass of CNTs in each slice (dm_i) per unit volume ($dv = t \times w \times dz$); z is the distance from the top of the forest to the forest slice; t is the CNT forest depth in the direction of the X-ray beam; I_0 is the X-ray intensity upstream of the CNT forest; I is the X-ray intensity downstream of the CNT forest; and μ/ρ is the total mass attenuation coefficient. The index is counted starting at the top of the forest, that is, for a 2 mm forest, $i = 200$ at the base.

The Beer–Lambert–Bouguer law is applicable for a homogeneous medium. This assumption is valid for the CNT forest because the waviness of the CNTs is on a much smaller length scale than the beam, and the variations in morphology (discussed later) occur over a much larger length scale. Throughout our analysis, we also assume that the forest is homogeneous in the $X-Y$ plane, that is, along the direction of the X-ray beam, which we have validated in previous work.[48]

For X-rays with energies below 20 keV, absorption is the primary contribution to X-ray attenuation, compared to both elastic and inelastic scattering. Hence, using the absorption mass attenuation coefficient instead of the total mass attenuation coefficient would have only resulted in a small error in the density calculation. Further, because there is only a small amount of absorption compared to the overall X-ray intensity (*i.e.*, $I_0 \approx I_i$), noise in the measurements leads to an apparent fluctuation in the calculated vertical profile of density. We estimate that the signal-to-noise ratio (SNR) of density measurements is equal to ≈2. The SNR is calculated as the ratio between the mean and the standard deviation (Figure S2D). Nevertheless, due to the high spatial resolution of our mapping technique, this noise is inconsequential when the local

density measurements are integrated as discussed later.

Using the mass density $\rho_m(z_i)$ of each slice with known thickness (Δz = 10 μm) and relating the slice mass (m_i) to the unit cross forest sectional area ($a = t \times w$), we calculate the areal mass density of each slice

$$m_a(z_i) = \rho_m(z_i)\Delta z \quad (2)$$

Next the cumulative areal density (m_{ac}, total CNT mass per unit area) *versus* position in the forest is calculated by summing the areal density of all slices

$$m_{ac}(z_i) = \sum_0^i \rho_m(z_i)\Delta z \quad (3)$$

The areal mass density per slice represents how much CNT mass was created for that specific 10 μm of the forest, and the cumulative areal density represents the mass of the CNT forest above (and including) the indexed slice.

We performed X-ray mapping of tall CNT forests (up to 2 mm) grown in both cold-wall (heated substrate, Absolute Nano SabreTube) and hot-wall (heated tube, Thermo-Fisher MiniMite) systems (Figure S1). Each forest was discretized into up to 200 slices with 10 μm thickness by scanning the X-ray beam vertically, as shown in Figure 2A,B. The mass density varies throughout the forest (Figure 2C,D): it increases in a closely linear trend from the top surface ("crust") of the forest until it reaches a maximum and brief plateau, then it decays gradually toward the bottom of the forest. The formation of a tangled crust at the start of growth is well-known; however, this density map reveals, for the first time, a subsequent "crowding" stage where the CNT density increases substantially as new CNTs begin to grow even long after the forest self-organizes and starts to thrust upward. The distance of this density increase (≈300 μm) is significantly larger than the nonuniformity of the top surface of the forest (Figure 2A,B), which we estimate to be less than 100 μm (Figure S3), and larger than any errors expected from sample tilt or beam divergence, which we estimate to be less than 50 μm (Figure S2B). Also, the employed alignment procedure (Figure S4), utilizing X-ray intensity scans ensures that the sample tilt (about *y*-axis) is within ≈0.01° of the substrate plane. Hence, the slope of the density increase predominately represents the kinetics of the crowding stage, that is, the rate at which new CNTs begin growing from catalyst particles that were inactive during the self-organization stage. Even considering the nonuniformity of the top surface and the beam divergence, the measured CNT density increase during crowding would be at least 5-fold.

We also observe that the kinetics of crowding depends on the process conditions, suggesting that the rate of crowding and the maximum density represent the efficiency of CNT nucleation from the population of

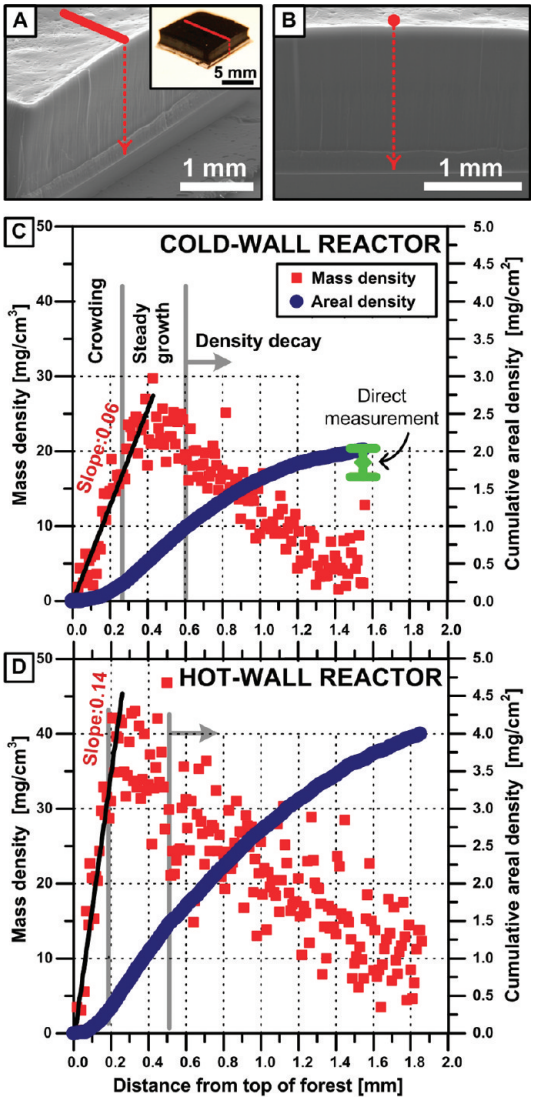

Figure 2. (A,B) SEM images of uniform forest structure for a sample grown in the cold-wall reactor. Red line indicates the path of the X-ray beam scanned vertically through the middle of the forest. Inset in A: Photograph of the same forest. Spatial evolution of mass density and areal density for CNT forests grown in (C) cold-wall reactor with resistively heated substrate; (D) hot-wall reactor with externally heated quartz tube.

catalyst particles on the substrate. For instance, as can be seen by comparing Figure 2C,D, the slope of CNT density increase for the sample grown in a hot-wall reactor is approximately twice that of the sample grown in a cold-wall reactor. We attribute this to the different process parameters used in the two systems, which are documented in Figure S1 (Supporting Information). Both samples were annealed at 775 °C in H_2/He; however, the rate of heating and duration of annealing in the cold-wall system was much shorter than that in the hot-wall system. A long annealing duration may be necessary for catalyst nanoparticles to be fully reduced from a higher oxide state (Fe^{2+} or Fe^{3+}) to a lower one (Fe^{1+} or Fe^0) in order to become active.[55,56] This could also explain why the hot-wall

sample has a higher maximum density, indicating that a larger fraction of the catalyst nanoparticles becomes active for CNT growth.

After the maximum density is reached, the density remains approximately constant at this value for a small (≈300 μm or less) portion of the forest (<20% of the forest height). Hence, only a small portion of the forest is truly uniform, and this observation may highlight the general difficulty of producing highly uniform and tall CNT ensembles even though many CVD methods of growing millimeter-scale CNT forests have assumed overall uniformity. Then, after the brief steady growth stage, the density decays due to accumulated deactivation of individual catalyst particles and proceeds until eventual self-termination. The shape and/or the slope of the decay also depends on the growth conditions, representing variability in the catalyst deactivation kinetics. Nevertheless, a universal observation in all samples we have tested is that both the initial density at the top of the forest (including the crust) and the final density are approximately 1 order of magnitude below the maximum density. Thus the same critical CNT density forms the self-supporting structure that enables "lift-off" of the CNT forest and causes collective self-termination at the end of the growth process.

The spatial evolution of the cumulative areal mass density (mg/cm^2) is also shown in Figure 2. The last point on this curve corresponds to the bottom of the forest and therefore represents the total areal density of the sample. For the cold-wall forest, we compare this value to a direct measurement of the CNT forest mass which was measured using a microbalance. We therefore confirm that the calculated density value based on X-ray mass attenuation is very close to the true density. Using thermogravimetric analysis (TGA), shown in Figure S5, we find that the contribution of amorphous carbon and any other low evaporation temperature carbonaceous contaminants is limited to about 10% of the total mass of this sample (recipe in Figure S1). Hence, the mass measurements are dominated by CNTs rather than carbonaceous impurities.

The cumulative areal density follows an S-shaped curve with increasing distance from the top crust. This shape is explained by the spatial evolution of local mass density along the forest height. The initial acceleration (concave up region) in the cumulative areal density results from the newly identified crowding stage, and the deceleration (concave down region) results from the density decay stage. The intermediate steady growth stage results in an approximately linear relationship between total mass and vertical position.

Now, we proceed to analyze the population dynamics within the forest based on spatial mapping of the CNT diameter and alignment. This information is necessary to build a comprehensive picture of the forest internal structure and is needed to calculate the evolution of CNT number density. Then, these results are combined with real-time height kinetics to calculate the time evolution of forest mass and density. Because real-time height kinetics can only be measured during growth in the cold-wall system, the remainder of analysis in this paper uses results from the cold-wall growth process.

Although transmission electron microscopy (TEM) has been customarily used for measuring CNT diameters and number of walls,[5,6] it is painstaking to obtain reliable descriptive statistics from measurements of a limited number of CNTs, compared to the inherent ability of SAXS to probe at least 10^6 CNTs in the beampath. It is also perhaps impossible to do accurate spatial profiling of size distributions using TEM at the high spatial resolution (10 μm) enabled by the capillary optics used with our SAXS setup. Analysis of the radial breathing modes (RBM) using two-wavelength *in situ* Raman spectroscopy has been used to obtain the diameter distribution of single-walled CNTs (SWNTs);[57] however, this is only suitable for SWNTs, or double-wall CNTs (DWNTs), within an incomplete diameter range, and it requires that the CNTs be resonant with the incident laser energy. On the other hand, X-ray scattering methods inherently enable characterization of any CNT based on its dimensions.

Hence, we use the X-ray scattering 2D image collected on the area detector (Figure 1A) to map the CNT size distribution by fitting the peak (or shoulder) observed in a linescan with a mathematical form factor model for hollow cylinders[28,48,49] having a log-normal distribution of diameters (Figure S6). Figure 3A shows the SAXS $I-q$ profiles along with model fits for forest slices selected every 0.1 mm throughout the forest height. This model-fitting procedure is repeated for each of the 156 slices (images) for the studied forest, resulting in a spatial map with unprecedented resolution compared to previous studies of CNT forest morphology.[1,5,6,28,49,58] Because of the large number of images, we developed an automated algorithm for choosing the fitting range based on the key features of the linescan, as described in Figure S7. The blue marks in Figure 3A indicate the lower and upper limits for the fitting range and the peak (shoulder) position determined using this algorithm. A trend of decreasing CNT outer diameter (CNT OD) can be inferred from the position of the peak (or a shoulder in cases in which there is no well-defined peak) relative to the inverse space parameter q because the peak (or shoulder) position correlates inversely with CNT diameter. The peak moves from $q \approx 0.75$ to 0.9 nm^{-1} (≈20% increase) from top to bottom of the forest.

As seen in Figure 3, the mathematical model provides excellent fits to the scattering data, throughout the forest. The probability density functions (PDFs) of CNT OD distribution for each forest slice are laid together in Figure 3B, along with the normalized histogram of CNT OD measurements collected using

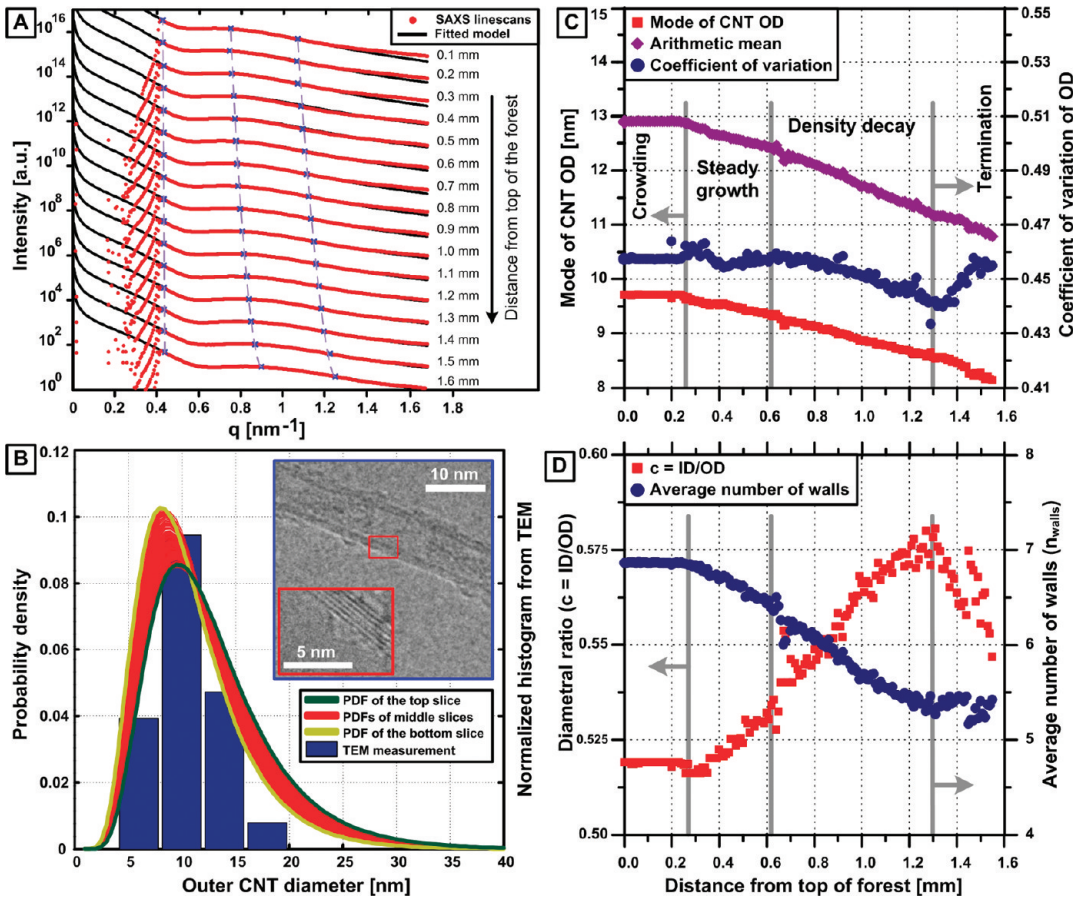

Figure 3. Spatial mapping of CNT dimensions and polydispersity throughout a CNT forest: (A) selected linescans from SAXS images, compared to fits using scattering model (there are nine images between each of the locations shown here); (B) comparison of the CNT OD distributions (fitted PDFs) to a normalized histogram of measurements from TEM images (example as inset); (C) mode, arithmetic mean, and coefficient of variation of CNT OD, calculated for each beam position ("slice") in the forest; (D) diameter ratio (*c*) and average number of walls for each slice.

TEM. There is a good agreement between the diameter values as well as the PDF obtained from SAXS fitting with TEM measurements, validating the accuracy of the SAXS measurement technique.[28,49] The inset to Figure 3B shows a TEM micrograph of a representative CNT with six walls. The smoothness of the spatial trends of CNT dimensions and their variance highlights the precision of our technique because the mathematical model fit produces a highly confident and accurate result for each slice. Also, the resolution of size measurement is effectively atomic because a scattering model is based on the coherent elastic interactions between X-rays and carbon atoms forming the CNTs. Due to the large number of scatterers (atoms of more than 10^6 CNTs) in the beampath through the CNT forest, high confidence descriptive statistics are obtained.

As shown in Figure 3C, the mode of CNT OD shifts from 9.7 to 8.1 nm as growth proceeds (from top to bottom of the forest), which is a 16.5% decrease, and the arithmetic mean shifts from 12.9 to 10.8 nm, which is a 16.3% decrease. The difference between the mode and arithmetic mean highlights the skewness of the log-normal distribution of the CNT population throughout the forest.

In spite of the overall decay in CNT diameter during growth, we find that both the CNT OD and its coefficient of variation (CV) are constant during the crowding stage when the CNT number density increases to the maximum. This shows that the density increase represents an increasing population of active (*i.e.*, CNT-bearing) catalyst particles with an invariant diameter distribution. In other words, there is no preferential nucleation of smaller or larger diameter CNTs within the population under the tested growth conditions (Figure S1). After the crowding stage, the CNT OD decreases until growth stops, and the CV decreases until the onset of the termination stage at which time the CV increases rapidly until growth stops. During the termination stage, the corresponding lowest part (base) of the forest exhibits significant broadening of the diameter distribution. This broadening, along with a continued decrease of the mode and mean OD, may suggest that growth of larger diameter CNTs is halted more abruptly during collective termination. Although the forest height abruptly stops increasing when the CNT density drops below the critical threshold, smaller diameter CNTs may continue to grow and attempt to

push up into the forest.[59] This can also explain the shifts in the OD and CV values in the termination region.

Another parameter of the CNT scattering model is the diameteral ratio (c = ID/OD), which is the ratio between the average inner diameter (ID) and outer diameter (OD). This enables calculation of the average number of CNT walls (n_{walls}), shown in Figure 3D. The number of walls is unchanged during crowding, then decreases from ≈7 to 5 walls during density decay and remains fairly constant through the termination stage as a result of the decay in both the CNT OD and the diametral ratio (c). These changes can perhaps be linked to the morphological evolution of the catalyst nanoparticles, which is discussed later.[4,60]

Now, the CNT number density profile (*i.e.*, the total number of CNTs at each vertical position) can be calculated by combining the profiles of areal mass density and the measured CNT dimensions. However, owing to the skewness of the log-normal distributions, a single value OD (mean or mode) cannot be used in this calculation; that is, the average CNT mass of a skewed population is not equal to the mass of CNTs having the average diameter. Hence, the entire PDF must be used to assign the proportion of the population that belongs to a specific narrow bin of diameters, and we must also correct for the CNT tortuosity by calculating the corrected CNT length from alignment and height data for each slice.

Accordingly, the CNT OD range of 5−40 nm is divided up into small diameter bins of width ΔD_{bin} = 0.5 nm. Now, the ratio between the number of CNTs within each bin $N(D_o)$ centered at the outer diameter D_o and the total number of CNTs (N_i) within each forest slice is calculated from the PDF of each slice i

$$\left(\frac{N(D_o)}{N_i}\right) = \int_{D_o - \Delta D_{bin}/2}^{D_o + \Delta D_{bin}/2} \mathrm{PDF}_i \mathrm{d}D \tag{4}$$

To accurately calculate the total volume of the tortuous CNTs within each slice and therefore calculate the mass, we must know the actual CNT length rather than just the height of the slice. So, we calculate a height-to-length transformation factor based on the CNT alignment within each slice. To quantify the CNT alignment, we use the orientation parameter (f) calculated from azimuthal scans at the q location of maximum intensity[1,3,48,49,61]

$$f(z_i) = \frac{1}{2}(3\langle \cos^2 \phi \rangle_i - 1) \tag{5}$$

where

$$\langle \cos^2 \phi \rangle_i = \frac{\int_0^{\pi/2} (I_i(\phi) \sin \phi \cos^2 \phi) \mathrm{d}\phi}{\int_0^{\pi/2} (I_i(\phi) \sin \phi) \mathrm{d}\phi} \tag{6}$$

Here, ϕ is the angle between the CNT direction and the z-axis direction, and $I_i(\phi)$ is the azimuthal intensity distribution of scattered X-rays from the SAXS image of slice i.

A transformation factor (Λ) is then calculated to convert the apparent forest height (slice thickness Δz) to the average CNT length (Δl) within that slice[3]

$$\Delta l(z_i) = \Lambda(z_i)\Delta z \tag{7}$$

where

$$\Lambda(z_i) = \left(\frac{3}{2f(z_i)+1}\right)^{1/2} \tag{8}$$

Now, we can calculate the total number of CNTs within each slice (N) by dividing the previously calculated (eq 2) mass of each slice (m_a) by the weighted average mass of a CNT (m_{CNT}) of the population based on the obtained PDF of CNT OD distribution and using the corrected average CNT length (Δl) in each slice. This follows as

$$N(z_i) = \frac{m_a(z_i)}{m_{CNT}(z_i)} \tag{9}$$

where

$$m_{CNT}(z_i) = \rho_g \Delta l(z_i) \sum_{D_o = 5\mathrm{nm}}^{D_o = 40\mathrm{nm}} \left(\left(\frac{N(D_o)}{N_i}\right)\frac{\pi}{4} {D_o}^2 (1 - c(z_i)^2)\right) \tag{10}$$

The bulk density is taken as the value for graphite, ρ_g = 2.2 g/cm^3.

The orientation parameter $f(z_i)$ and the height-to-length transformation factor are shown in Figure 4A. The tangled top "crust" layer is typically no more than a few micrometers thick; however, the first points of the X-ray map are affected by non-uniformity in the top surface of the forest. As a result, there is an apparent slight decrease of the orientation parameter at the top of the scan, until the beam has passed through the non-uniform region. After this, the orientation parameter increases to a maximum at the end of the steady growth stage, then decreases gradually through the density decay stage, and then decreases rapidly during the termination stage. The transformation factor varies inversely (eq 8) with the orientation parameter and therefore is greatest at the top and bottom of the forest.

We can now derive the profile of CNT number density *versus* position, which is shown in Figure 4B. The number density increases during crowding, reaching a maximum of ≈9 × 10^9 CNTs/cm^2, and then decays. The maximum is about an order of magnitude higher than the initial density and then decreases by about an order of magnitude before termination. Compared to the mass density profile (Figure 2C), the number density profile is curvier and less steep due to the diameter change and the tortuosity correction of CNT length. In spite of the noise in the X-ray density measurements, we suggest that the beginning and ending CNT number density values represent the critical value for the self-supporting structure. The

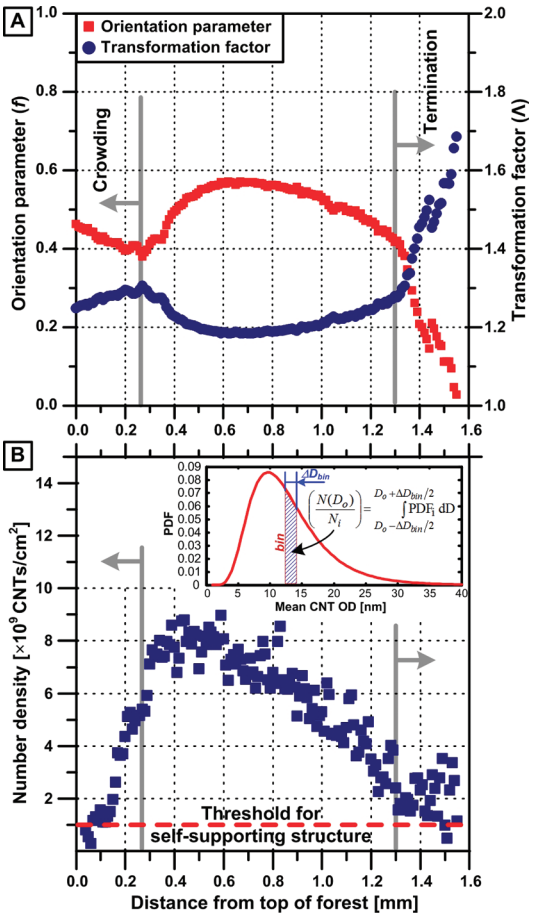

Figure 4. Determination of the CNT population kinetics: (A) spatial map of the orientation parameter and the height-to-length transformation factor; (B) spatial map of CNT number density, calculated using the CNT diameter distribution and the tortuosity-corrected average CNT length for each slice. Inset to (B) describes calculation of the total number of CNTs from the PDF of CNT OD for each slice.

horizontal red line marks the estimated threshold value (≈10^9 CNTs/cm^2) based on a finite element model of postbuckling behavior of CNTs in contact.[1]

Combining these spatial mapping results with the real-time forest height measurements (dz/dt) obtained *in situ* during growth, we determine the time evolution of CNT length, number density, and, more importantly, cumulative areal density (mass per unit area). The lengthening kinetics $l(t_i)$, the cumulative areal density kinetics $m_{ac}(t_i)$, and the total number density kinetics $N(t_i)$ are calculated

$$l(t_i) = \int_{t=0}^{t=t_i} \Lambda\left(\frac{dz}{dt}\right) dt \qquad (11)$$

$$m_{ac}(t_i) = \int_{t=0}^{t=t_i} \frac{dm_a}{dz}\left(\frac{dz}{dt}\right) dt \qquad (12)$$

$$\frac{dN(t_i)}{dt} = \left(\frac{dN(z_i)}{dz}\right)\left(\frac{dz}{dt}\right) \qquad (13)$$

In Figure 5, the CNT lengthening kinetics is compared to the height kinetics, showing that the measurements

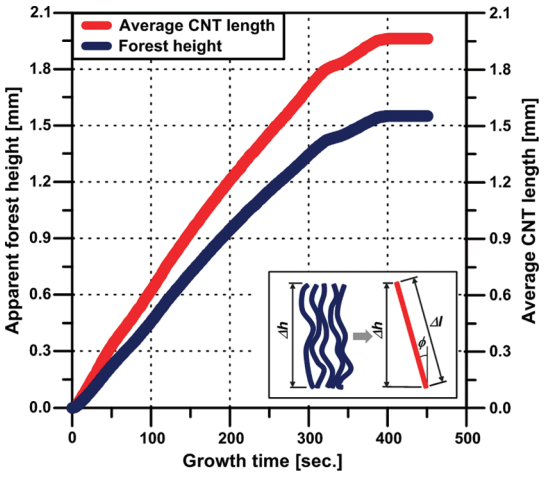

Figure 5. Kinetics of apparent forest height and corrected CNT length. Inset is a schematic of the height-to-length transformation.

of apparent forest height significantly underestimate the actual CNT length. Owing to the initial increase followed by a decrease in the orientation parameter across the forest, the slightly sublinear curvature of the apparent height kinetics becomes more linear when transformed into true CNT length.[3] Nevertheless, the evolution of forest mass is a more accurate measure of reaction kinetics, as it directly represents the rate at which carbon is incorporated in the growing CNT population. Incidentally, we observe that, for the same growth conditions, the areal mass density of CNT forests (*i.e.*, the total mg/cm^2) is more repeatable than the forest height or the volume density (mg/cm^3). In other words, for the same growth time, many grown forests may have a considerable variation in height, but the mass output of each experiment is more consistent (Figure S9).

Therefore, the culmination of our comprehensive analysis is a measure of the time evolution of the total cumulative areal density and the total CNT number density, shown in Figure 6. Due to the nearly linear height kinetics, both curves closely resemble the spatial profiles shown in Figures 2 and 4, and the total CNT forest mass *versus* time is an S-shaped curve. In addition, by processing atomic force microscopy (AFM) images, we calculate the mean number density of nanoparticles (Figure S10) on samples annealed according to the recipe in Figure S1 to be ≈8 × 10^{10} particles/cm^2 (about 2 orders of magnitude higher than the CNT lift-off threshold ≈10^9 CNTs/cm^2, identified in Figures 4 and 5). As shown in Figure 6, this results in a calculated catalyst activity that increases from ≈1 to ≈11% at the maximum CNT density during the steady growth stage.

The significant spatial variations in CNT morphology during growth confirm that the apparent forest height depends on the interplay between CNT number density, diameter, stiffness, tortuosity, and possibly the hierarchal bundling structure. However, many previous

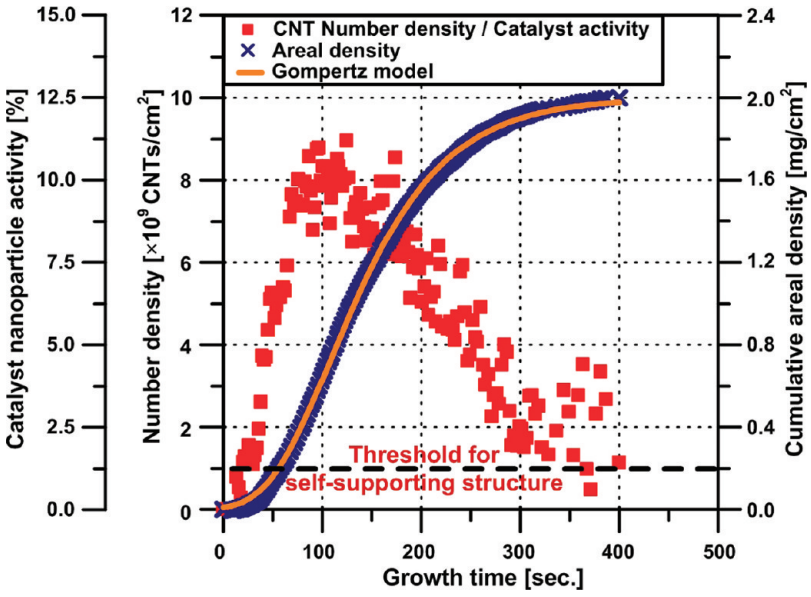

Figure 6. Time evolution of the CNT number density, catalyst activity, and cumulative areal density, which is fitted with the Gompertz population growth model.

studies that have represented CNT growth kinetics by forest height, and less commonly by forest mass, have found an S-shaped growth curve. Some have identified its key features including an initial acceleration,[39,44,45,62] an inflection point, and a deceleration that concludes in termination.[26,27,29,44,45,62−64] In general, growth models for individual CNTs and CNT−particle systems have been used to interpret these stages. The initial acceleration has been explained by the presence of an incubation/induction stage, in which the processes of carburization of the catalyst particles and nucleation of CNTs were proposed to exhibit an autocatalytic nature.[45] The final decelerating part was explained by catalyst deactivation kinetics based on various limiting mechanisms, such as catalyst poisoning, overcoating, evaporation, or diffusion.[4,23,29,32,65] However, the noted discrepancy between CNT forest height and mass, along with the frequent reliance of sparse (*i.e.*, *ex situ* time points) data to fit height kinetics to different kinetic models without obtaining representative statistics, highlights the importance of obtaining a population-based picture of the growth kinetics. An ideal model of CNT forest growth would therefore consider a distribution of individual growth behaviors and how these behaviors result in a drastic variation in CNT density throughout the growth process, which results in the observed true kinetic behavior of the population.

To obtain further insight about the S-shaped reaction kinetics, we investigated three known models that are ubiquitous to analysis of population growth in natural systems: the monomolecular model (eq 14), the autocatalytic model (eq 15), and the Gompertz model (eq 16)[66,67]

$$m_a(t) = \alpha\left(1 - e^{-k(t-\tau)}\right) \quad (14)$$

$$m_a(t) = \frac{\alpha}{1 + e^{-k(t-\tau)}} \quad (15)$$

$$m_a(t) = \alpha e^{\left(-e^{-k(t-\tau)}\right)} \quad (16)$$

In these models, α is the asymptotic final cumulative mass of growth, k is a reaction rate, and τ is the time origin.

We find that the Gompertz model is an excellent fit to the CNT mass kinetics in Figure 6 and compare all three fits in Figure S11. In fact, only the monomolecular (aka exponential decay) model was previously used to fit CNT growth data.[29] While the monomolecular model fits the decay part of the cumulative mass kinetics, the model fails to fit the initial accelerating part because it does not have an inflection point. On the other hand, both the autocatalytic and Gompertz models are sigmoidal equations that have inflection points. Further, the autocatalytic curve is symmetric about the inflection point, while the Gompertz curve is asymmetric. Hence, the Gompertz model fits our data best because the different rates of acceleration (crowding) and deceleration (decay) can be accommodated by the asymmetry of the curve (Figure 5B).

The Gompertz model has been extensively applied to population growth in animal systems[66] and has been applied to tumor growth[68] and bacterial growth.[69] It has also been recently used to represent the fibrillization kinetics of filamentous aggregates of τ proteins.[70] This analogy can give insights into possible competition among the population of growing CNTs because tumor growth involves a population of cells that grows in a confined space, with a limited supply of nutrients. While it is possible that catalyst deactivation and density decay in CNT forest growth analogously result from shortage of necessary growth precursors at the

catalyst,[30,71] this study as well as previous studies[25,29,72] show that growth is not strictly governed by the diffusion-limited mathematical model ($h \propto t^{1/2}$). Further, diffusivity through a forest changes during growth because of the evolution of CNT density, indicating that a modification to this model is needed in order to test the hypothesis that growth is purely diffusion-limited.

Alternatively, we hypothesize that growth kinetics is essentially a superposition of two different kinetics: activation and deactivation of catalyst nanoparticles. The deactivation rate eventually supersedes the continuous activation rate that dominates during the initial crowding stage. The asymmetry around the inflection point, as well as the catalyst lifetime, may be controlled by changing the growth conditions, affecting this activation−deactivation competition. Thus, we explain that the ubiquitous growth-enhancing agents, such as water or ethanol, can result in high overall catalyst activity and lifetime[2,73−80] by manipulating the rates of activation and deactivation. This may be done by manipulating the gas-phase chemistry and influencing migration of catalyst on the substrate.[2]

Our interpretation is also consistent with findings that reaction products and intermediates can contribute to the CNT growth rate either by reacting directly with the catalyst[45,81,82] or by co-reacting with other gas species.[83] For instance, the decomposition of hydrocarbon gas (C_2H_4 in our case) may be catalyzed by products or intermediates expelled from the dissociation reactions at the catalyst, even if they are unstable groups or short-lived free radicals. Thermal decomposition and rearrangement of C_2H_4 and H_2 is a multistep chain of gas-phase reactions yielding a plurality of compounds,[84] and in light of the sigmoid-shaped population kinetics, it is possible that some of these reactions manifest an autocatalytic nature and, depending on the product/compound, contribute to activation or deactivation of CNT growth. For instance, while alkynes have been specifically shown to accelerate CNT growth,[83] PAHs (precursors to soot) are also generated in thermal CVD, and there are many other compounds that are apparently benign. CH_2 was also identified as a possibly active species.[85] Measurements of the time-varying concentrations of both reactants and products will give further insights into the chemical causes and effects of changes in the density of growing CNTs.

Regardless of the exact interplay or competition between these compounds and mechanisms, termination of CNT growth is currently inevitable because the deactivation rate eventually dominates. In fact, this deactivation has been attributed to various mechanisms that are consequential of the gas-phase chemistry such as catalyst poisoning,[29] overcoating with amorphous carbon,[32] or steric hindrance,[45,86] indicating that manipulating the gas chemistry is an attractive route

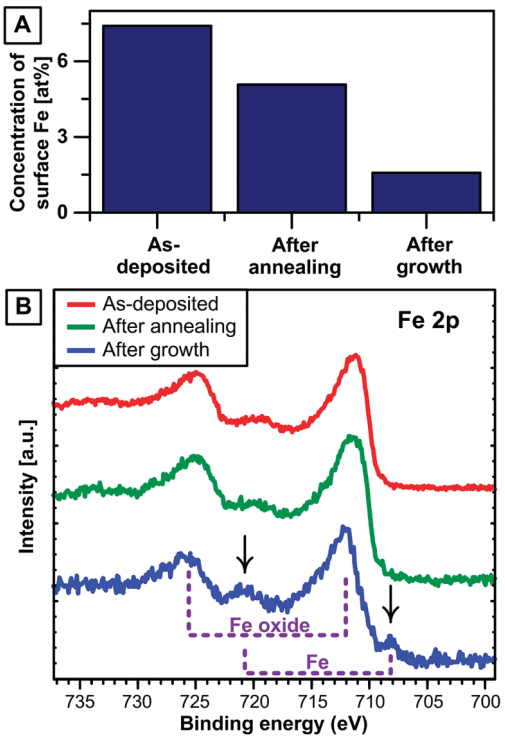

Figure 7. XPS analysis of catalyst evolution during annealing and growth: (A) atomic concentration of surface Fe based on the areas under the peak of Fe2p peaks of the survey spectra (Figure S12) for three samples (as-deposited, after annealing, and after growth); (B) comparison of normalized $Fe2p_{1/2}$ and $Fe2p_{3/2}$ peaks for samples as-deposited, after annealing (10 min ramp-up to 775 °C and hold for 10 more min), and after growth (for 15 min at 775 °C) and CNT delamination. To calibrate binding energy values, these spectra were shifted by +3.2 eV based on the measured C1s peak location (Figure S13).

for controlling deactivation. Another universal observation from our work, as well as others,[85] is that carbonaceous deposits on reactor walls from previous growth cycles can improve CNT nucleation and growth, possibly due to the presence of active species that desorb from the reactor wall surface when the furnace tube is heated.[85]

CNT growth deactivation can also be influenced by morphological evolution of catalyst nanoparticles such as by migration[1,4,21] and coarsening.[4,21,87] In our system, we hypothesize that accumulating CNT deactivation is in large part due to evolution of the catalyst particles, especially atomic diffusion of the catalyst into and beyond the supporting alumina layer.[4,21] Indeed, using *ex situ* X-ray photoelectron spectroscopy (XPS), as well as Rutherford backscattering spectroscopy (RBS) (results not shown), we observe significant diffusion of Fe catalyst into the substrate in samples that are processed in the hot-wall reactor. Figure 7A quantifies changes in the percentage of surface Fe after annealing and after growth (and delamination of the CNT forest), based on the area under the Fe2p peaks from survey scans (Figure S12). While the Fe concentration after growth and delamination can possibly be affected by

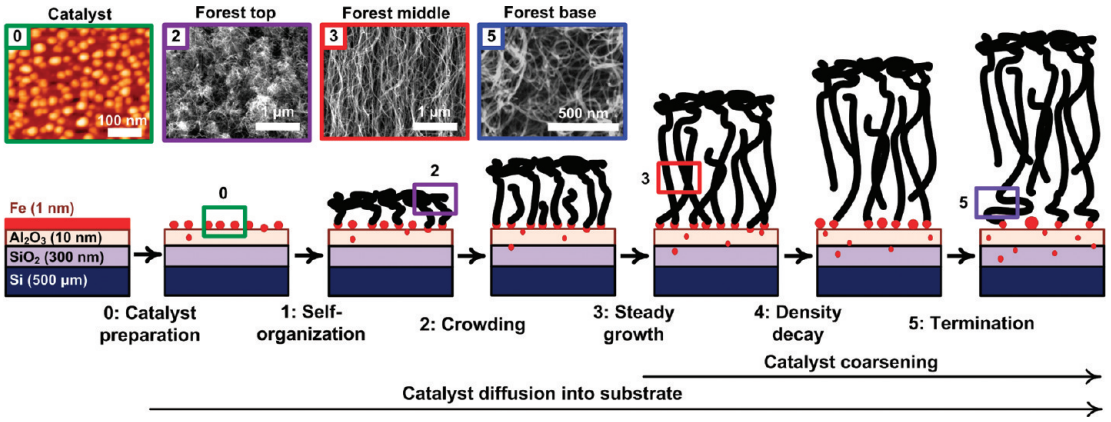

Figure 8. Collective model of catalyst evolution and CNT population dynamics, showing five distinct stages of the forest growth process identified by X-ray mapping, along with AFM image of the catalyst nanoparticles (stage 0, catalyst preparation), and SEM images of the tangled top (stage 2, crowding), aligned middle (stage 3, steady growth), and disordered base (stage 5, termination) of a typical forest grown by thermal CVD. Stage 2 shows how new CNTs begin growing after the forest self-organizes, and stage 4 shows how the density of CNTs decays until the critical threshold for self-termination is reached.

mechanical removal of some catalyst particles (*i.e.*, attached to the CNTs), the significant loss of Fe after annealing is evidence of catalyst diffusion through subsurface layers because the annealing temperature (775 °C) is not high enough to cause evaporation of the Fe catalyst. Nevertheless, in this base growth process, the catalyst nanoparticles are bound by strong interactions between Fe and Al_2O_3,[21,88] as demonstrated in literature for similar growth systems by means of backscatter electron imaging that showed no traces of metal particles on the top of grown CNT forests.[32]

Figure 7B is a superposition of the Fe2p spectral lines for three different samples (as-deposited, after annealing, and after growth). All spectra were collected during the same run and are plotted after applying a correction factor for line positions in order to accurately compare the binding energy values of spectral lines. A correction factor of +3.2 eV is calculated based on the commonly used value of 285 eV for the binding energy of the ubiquitous C1s peak (Figure S13). Results show that there is no significant change in the binding energy of the $Fe2p_{3/2}$ and $Fe2p_{1/2}$ lines ($2p_{3/2}$ peak remains at about 711.7 eV), indicating that Fe is in essentially the same oxidation state on all three samples. This is likely a combination of F^{2+} and F^{3+} based on the corrected binding energy values[34,55,56,89] and the asymmetry of the peaks. This can be attributed to the ambient oxygen exposure[90] after annealing and after growth which results in oxidation of Fe even if it was reduced to metallic Fe during the high-temperature process. Nevertheless, the appearance of a low binding energy $Fe2p_{3/2}$ peak at 708.2 eV indicates that there is some metallic Fe that did not oxidize upon exposure to atmosphere because it is trapped beneath the surface. Notably, after subsequent heating in a reducing environment of H_2/He, this peak becomes more significant, while after heating in air, the peak completely disappears (results not shown). Also, after heating in H_2/He, there is no shift in the C1s peak position (Figure S13), and we find (Figure S12) that the carbon signal decays while the aluminum signal increases after growth. These observations indicate that the low binding energy $2p_{3/2}$ peak in fact represents subsurface metallic Fe and not iron carbide or Fe particles encapsulated with graphitic carbon. Because XPS penetrates only a few nanometers into the sample, these findings can only prove the diffusion of Fe to the near subsurface Al_2O_3 layer, although we hypothesize that Fe could also diffuse to the SiO_2 layer.

On the basis of population analysis enabled by high-resolution X-ray mapping and the observation of catalyst migration into the substrate, we present a unified picture of the successive stages of CNT forest growth in Figure 8. This picture begins with the catalyst preparation stage by dewetting of a thin Fe film (1 nm thick) to form nanoparticles. In separate work where we have studied the dewetting process using *in situ* grazing incidence X-ray scattering,[87] we observe that the kinetics of particle formation is very fast; that is, the Fe film dewets almost immediately when the temperature reaches a certain value during rapid heating. After this, the particle size and shape are fairly stable by the time the hydrocarbon gas is introduced.[87] Hence, the crowding of CNTs during and after self-organization occurs over a much longer time scale than particle formation. Also, as can be seen in Figure 3, the CNT diameter distribution does not change during crowding, indicating that catalyst size evolution is an even longer time scale process. The finding that activation of the catalyst population occurs at an increasing rate evokes thoughts of popcorn (CNTs) popping from a defined population of kernels (particles).[91] The nucleation kinetics of the CNT population is likely dependent on the hydrocarbon gas decomposition, surface

carburization, and other processes and may reflect an autocatalytic behavior.

After the brief steady growth stage that follows crowding, the CNT density decays gradually and for a long duration, resulting in at least an order of magnitude decrease in active population of CNT-bearing catalyst particles. The density decay is accompanied by a decrease in the average CNT diameter and a focusing of the diameter distribution. Finally, the collective termination stage is represented by a rapid loss of alignment and a widening in the CNT diameter distribution as discussed earlier. Collective termination occurs when the forest is no longer sufficiently dense to maintain a self-supporting structure, although it is likely that some CNTs continue to grow and push upward into the tangled base layer.[59]

In situ[87] and *ex situ*[4,92] studies showed that the average size of catalyst nanoparticles increases with successive exposure to a hydrogen atmosphere, presumably due to Ostwald ripening. Hence, there is a discrepancy between the evolution of catalyst size (increases) and the evolution of CNT size (decreases). We have also noticed in repeated growth experiments (*i.e.*, growth, delamination, growth) from the same catalyst-coated substrate that the CNT forests have larger diameter and lower mass density in subsequent growth cycles. A possible explanation for the decreasing average CNT diameter within a single growth cycle is that larger diameter CNTs stop growing first; that is, smaller CNTs have a longer catalyst lifetime. A further important point is that not all catalyst particles grow CNTs, and in fact, only a small fraction of the catalyst particles may be active depending on the annealing and growth conditions. The catalyst activity measurements shown in Figures 6 indicate that the maximum CNT number density is ≈11% of the catalyst particle number density (Figure S10).

Hence, we must consider that the size evolution of catalyst particles that bear CNTs may be considerably different than particles that do not bear CNTs. It is plausible that the presence of a CNT constrains particle migration and atomic diffusion of Fe, and therefore particles with CNTs could have a more stable size distribution than particles without CNTs. Therefore, the ripening of the overall particle population could be dominated by the large subpopulation of particles that do not bear CNTs. In the limiting case that CNT growth rate does not depend on diameter (which is unlikely based on our recent results), and that CNT-bearing particles do not evolve by Ostwald ripening, the decrease of average CNT diameter with continued growth could be driven solely by a decrease in catalyst size caused by diffusion of Fe atoms into the substrate. While it is widely accepted that the catalyst nanoparticle size determines the CNT diameter,[62,93,94] there is no consensus on how an already nucleated CNT responds to size changes in the catalyst nanoparticle at its root, or how the presence of the CNT affects how the catalyst size changes. Indeed, the catalyst particle is highly dynamic under the thermal and mechanical conditions imposed by CNT growth,[60,95] and further study is required to understand how to stabilize catalyst particles for longer durations and overcome the several competing mechanisms of CNT growth deactivation. Also, the distribution of growth behaviors presented by our complete CNT population implies that a particular set of time-invariant growth process parameters may be optimal for only a small subpopulation, whereas the collective growth behavior is dominated by the response of the remainder of the population to the resulting suboptimal process parameters.

CONCLUSION

Understanding the population growth dynamics of individual nanostructures such as CNTs is vital to engineer materials comprising assemblies of nanostructures and to develop accurate models of their scale-dependent properties. We presented a comprehensive methodology for studying the population growth dynamics of vertically aligned CNT forests, utilizing high-resolution spatial mapping of synchrotron X-ray scattering and attenuation, along with real-time height kinetics. This methodology enables nondestructive calculation of the spatiotemporal evolution of absolute CNT mass and number density as well as CNT dimensions (diameter and number of walls). After the CNT forest self-organizes, the density increases during a crowding stage, and then the density decays almost an order of magnitude before self-termination occurs. The S-shaped mass kinetics is accurately fitted with the asymmetric Gompertz model of population growth; hence, CNT synthesis is governed by competing rates of activation and deactivation and is eventually limited by competing effects of gas-phase chemistry and catalyst evolution. This comprehensive picture of CNT population growth combines both chemical and mechanical cooperation throughout five distinct stages: self-organization, crowding, steady growth, decay, and collective termination.

Although all of the X-ray data in this paper were obtained *ex situ*, the same technique can be applied *in situ* to enable real-time monitoring of population behavior, enabling the control of the outcome by tuning the process parameters *in situ* either in an open loop or a feedback closed loop system. Such dynamic growth recipes will enable synthesis of CNT forests with highly uniform density or prescribed density gradients and possibly overcome collective termination to enable growth of indefinitely long CNTs. The population-based picture of CNT synthesis can be extended to bulk CNT growth processes from powder catalysts that also represent nanoparticle populations and is vital for manufacturing uniform CNT

materials by postprocessing, such as spinning,[20] rolling,[12] and transfer printing,[96] which are essential to integration of CNTs into functional materials and devices. Finally, our methodology and insights into the collective growth behavior of filaments can be generalized to study other systems of filamentary nanostructures including inorganic nanowires or biological filaments such as actin.[97]

METHODS

Forests of vertically aligned CNTs are grown using either a hot-wall reactor (tube furnace) or a substrate-heated cold-wall reactor that is equipped with real-time height monitoring (see Figure S1 in Supporting Information). In both cases, custom labVIEW interfaces were used to control process variable, such as temperature and gas flow rates. For the cold-wall reactor, the substrate temperature was measured by an infrared sensor (Exergen 2ACF-K-HIE). Digital mass flow controllers (Aalborg GFC 17, response time = 2 s) were used to control and measure gas flow rates. Real-time forest height is measured using a noncontact laser displacement sensor (LK-G152, Keyence) which is mounted above the cold-wall reactor as described earlier.[25,28] The substrate is a multilayer catalyst thin film (1 nm Fe/10 nm Al_2O_3/300 nm SiO_2) deposited by e-beam evaporation on 0.5 mm thick ⟨100⟩ 4 in. silicon wafer.

For X-ray scattering measurements, the CNT forest is placed on a motorized stage in the beampath of the G1 beamline at Cornell High Energy Synchrotron Source (CHESS). A beam energy of 10 ± 0.1 keV (wavelength ≈ 0.13 nm) is selected with synthetic multilayer optics (W/B4C, 27.1 Å *d*-spacing), and the beam is focused down to ≈10 μm using a single-bounce monocapillary that was fabricated at CHESS. The beam size is accurately measured by scanning the beam over a pinhole slit mounted on a motorized stage while measuring the beam intensity. The sample is aligned according to the procedure explained in Figure S4. Figure S2 shows a schematic and X-ray intensity readings from the X-ray detectors placed upstream and downstream of the CNT forest. The downstream X-ray intensity measurements are normalized to the upstream measurements in order to eliminate the effect of the drift in synchrotron intensity with time. Then the Beer–Lambert–Bouguer law is applied to calculate the mass density of each slice in the CNT forest, based on the total mass attenuation coefficient of carbon (graphite) at the X-ray energy of 10 KeV (≈3 cm^2/g).[98]

A standard sample of silver behenate powder (d_{001} = 58.380 Å) is used to calibrate the pixel-to-*q* ratio. Linescans from the 2D SAXS patterns are fitted using a mathematical model for log-normally distributed hollow cylinders (Figure S6). These scans are obtained by integration of intensities within ±10° from the reference direction (*x*-axis) of the inverse space parameter *q* (chosen to be the direction of maximum intensity). In order to automate the process of fitting for hundreds of scattering images, an algorithm was developed to select the fitting range of each scan and determine an approximate location of the peak based on the locations of the inflection points around the peak, as described in Figure S7. The fitting code used an iterative approach in searching for the best fit within this selected fitting range. By including the low *q* part of the data, a good fit was achieved that selects a probability density function (PDF) for diameter distribution as well as for the ratio *c* = ID/OD, where ID is the inner diameter of the multiwalled CNT and OD is the outer diameter of the multiwalled CNT (see Figure S8).

X-ray photoelectron spectroscopy (XPS) was carried out at room temperature on the substrate-bound catalyst for ≈5 × 5 mm samples. In all cases, samples were exposed to the atmosphere before putting them in the high-vacuum XPS chamber. A Kratos Axis Ultra X-ray photoelectron spectrometer was used with a monochromatic X-ray source (Al Kα X-ray radiation). The pass energy of the analyzer is 160 eV for the survey scans and 20 eV for the core scans. The anode voltage was set to 15 kV, and emission current to 6 mA (X-ray power ≈90 W). CasaXPS software (version 2.3.14) was used to process the spectra. All samples were placed together on the same sample holder, and spectra were collected back-to-back during the same run for comparative purposes (Figure S12). The carbon 1s peak is used to obtain an offset correction factor of +3.2 eV, based on the commonly used value of 285 eV for the carbon peak (Figure S13).

AFM imaging was done using MultiMode AFM, Nanoscope IIIa controller in tapping mode, and WSxM 3.0 Beta 12.1 software was used to view results.[99] A Matlab code was developed to further process AFM images in order to count the particle number density based on an algorithm that finds the local maxima of the intensity map representing the AFM image (Figure S10).

Acknowledgment. We thank Arthur R. Woll and Erik Polsen for help with X-ray scattering data collection, Teresa de los Arcos for valuable discussions concerning XPS characterization, and Namiko Yamamoto of MIT for preparation of catalyst substrates. Financial support was provided by the Department of Energy Office of Basic Sciences (model development, data analysis, and manuscript preparation) under Award DE-SC0004927, the Office of Naval Research (X-ray scattering measurements) under Award N000141010556, and the National Science Foundation (CNT sample preparation) under Award CMMI-0800213. X-ray scattering was performed in the G1 beamline at the Cornell High-Energy Synchrotron Source (CHESS), which is supported by the NSF and the National Institutes of Health under Grant DMR-0225180. Electron microscopy and X-ray photoelectron spectroscopy (XPS) were performed at the University of Michigan Electron Microbeam Analysis Library (EMAL).

Supporting Information Available: Details of the CVD reactors (hot-wall and cold-wall) used for CNT synthesis with respective schematics and growth recipes; the X-ray mass attenuation measurements and local density calculations; SEM images of the forest showing the flatness of the top surface and CNT morphology at different parts of the forest (top, middle, and bottom); sample alignment procedure; TGA of the same sample that was grown in the cold-wall reactor and was used for the analysis in the paper; the schematic and mathematical model used for fitting the linescans obtained from SAXS images by a population of hollow cylinders having a log-normal distribution of diameters; the algorithm developed for automating the selection process for the fitting range and determining an approximate location of the peak from SAXS linescans; the effect of the diameter ratio (*c*) on the fit of intensity curve in the low *q* range; mass density *vs* forest height for a number of CNT forest samples that were grown in a hot-wall reactor; the time evolution of the areal mass density (mass per unit substrate area) with fits from three different models: monomolecular model, autocatalytic model, Gompertz model; XPS survey spectra for three samples (as-deposited, after annealing, and after growth) collected together in the same run with annealing/growth recipes; XPS core spectra for C1s peaks for the same three samples; and analysis of the activity of catalyst nanoparticles based on processing AFM images to obtain mean particle number density for the same growth conditions of the sample grown in the cold-wall reactor. This material is available free of charge *via* the Internet at http://pubs.acs.org.

REFERENCES AND NOTES

1. Bedewy, M.; Meshot, E.; Guo, H.; Verploegen, E.; Lu, W.; Hart, A. Collective Mechanism for the Evolution and Self-Termination of Vertically Aligned Carbon Nanotube Growth. *J. Phys. Chem. C* **2009**, *113*, 20576–20582.

2. Amama, P. B.; Pint, C. L.; McJilton, L.; Kim, S. M.; Stach, E. A.; Murray, P. T.; Hauge, R. H.; Maruyama, B. Role of Water in Super Growth of Single-Walled Carbon Nanotube Carpets. *Nano Lett.* **2009**, *9*, 44–49.
3. Meshot, E.; Bedewy, M.; Lyons, K.; Woll, A.; Juggernauth, K.; Tawfick, S.; Hart, A. Measuring the Lengthening Kinetics of Aligned Nanostructures by Spatiotemporal Correlation of Height and Orientation. *Nanoscale* **2010**, *2*, 896–900.
4. Kim, S. M.; Pint, C. L.; Amama, P. B.; Zakharov, D. N.; Hauge, R. H.; Maruyama, B.; Stach, E. A. Evolution in Catalyst Morphology Leads to Carbon Nanotube Growth Termination. *J. Phys. Chem. Lett.* **2010**, *1*, 918–922.
5. Hasegawa, K.; Noda, S. Diameter Increase in Millimeter-Tall Vertically Aligned Single-Walled Carbon Nanotubes during Growth. *Appl. Phys. Express* **2010**, *3*, 045103.
6. Hasegawa, K.; Noda, S. Millimeter-Tall Single-Walled Carbon Nanotubes Rapidly Grown with and without Water. *ACS Nano* **2011**, *5*, 975–984.
7. Prasher, R. S.; Hu, X. J.; Chalopin, Y.; Mingo, N.; Lofgreen, K.; Volz, S.; Cleri, F.; Keblinski, P. Turning Carbon Nanotubes from Exceptional Heat Conductors into Insulators. *Phys. Rev. Lett.* **2009**, *102*, 105901.
8. Coleman, J. N.; Khan, U.; Blau, W. J.; Gun'ko, Y. K. Small but Strong: A Review of the Mechanical Properties of Carbon Nanotube−Polymer Composites. *Carbon* **2006**, *44*, 1624–1652.
9. Nirmalraj, P. N.; Lyons, P. E.; De, S.; Coleman, J. N.; Boland, J. J. Electrical Connectivity in Single-Walled Carbon Nanotube Networks. *Nano Lett.* **2009**, *9*, 3890–3895.
10. Wei, B. Q.; Vajtai, R.; Ajayan, P. M. Reliability and Current Carrying Capacity of Carbon Nanotubes. *Appl. Phys. Lett.* **2001**, *79*, 1172–1174.
11. Nihei, M.; Horibe, M.; Kawabata, A.; Awano, Y. Simultaneous Formation of Multiwall Carbon Nanotubes and Their End-Bonded Ohmic Contacts to Ti Electrodes for Future ULSI Interconnects. *Jpn. J. Appl. Phys.* **2004**, *43*, 1856–1859.
12. Tawfick, S.; O'Brien, K.; Hart, A. J. Flexible High-Conductivity Carbon-Nanotube Interconnects Made by Rolling and Printing. *Small* **2009**, *5*, 2467–2473.
13. Halonen, N.; Rautio, A.; Leino, A. R.; Kyllonen, T.; Toth, G.; Lappalainen, J.; Kordas, K.; Huuhtanen, M.; Keiski, R. L.; Sapi, A.; *et al.* Three-Dimensional Carbon Nanotube Scaffolds as Particulate Filters and Catalyst Support Membranes. *ACS Nano* **2010**, *4*, 2003–2008.
14. Valentini, L.; Armentano, I.; Kenny, J. M.; Cantalini, C.; Lozzi, L.; Santucci, S. Sensors for Sub-ppm NO_2 Gas Detection Based on Carbon Nanotube Thin Films. *Appl. Phys. Lett.* **2003**, *82*, 961–963.
15. Li, J.; Lu, Y. J.; Ye, Q.; Cinke, M.; Han, J.; Meyyappan, M. Carbon Nanotube Sensors for Gas and Organic Vapor Detection. *Nano Lett.* **2003**, *3*, 929–933.
16. Modi, A.; Koratkar, N.; Lass, E.; Wei, B. Q.; Ajayan, P. M. Miniaturized Gas Ionization Sensors Using Carbon Nanotubes. *Nature* **2003**, *424*, 171–174.
17. Qian, H.; Greenhalgh, E. S.; Shaffer, M. S. P.; Bismarck, A. Carbon Nanotube-Based Hierarchical Composites: A Review. *J. Mater. Chem.* **2010**, *20*, 4751–4762.
18. Zhang, M.; Fang, S. L.; Zakhidov, A. A.; Lee, S. B.; Aliev, A. E.; Williams, C. D.; Atkinson, K. R.; Baughman, R. H. Strong, Transparent, Multifunctional, Carbon Nanotube Sheets. *Science* **2005**, *309*, 1215–1219.
19. Zhang, M.; Atkinson, K. R.; Baughman, R. H. Multifunctional Carbon Nanotube Yarns by Downsizing an Ancient Technology. *Science* **2004**, *306*, 1358–1361.
20. Kuznetsov, A. A.; Fonseca, A. F.; Baughman, R. H.; Zakhidov, A. A. Structural Model for Dry-Drawing of Sheets and Yarns from Carbon Nanotube Forests. *ACS Nano* **2011**, *5*, 985–993.
21. Amama, P. B.; Pint, C. L.; Kim, S. M.; McJilton, L.; Eyink, K. G.; Stach, E. A.; Hauge, R. H.; Maruyama, B. Influence of Alumina Type on the Evolution and Activity of Alumina-Supported Fe Catalysts in Single-Walled Carbon Nanotube Carpet Growth. *ACS Nano* **2010**, *4*, 895–904.
22. Kim, D. H.; Jang, H. S.; Kim, C. D.; Cho, D. S.; Yang, H. S.; Kang, H. D.; Min, B. K.; Lee, H. R. Dynamic Growth Rate Behavior of a Carbon Nanotube Forest Characterized by *In Situ* Optical Growth Monitoring. *Nano Lett.* **2003**, *3*, 863–865.
23. Puretzky, A. A.; Geohegan, D. B.; Jesse, S.; Ivanov, I. N.; Eres, G. *In Situ* Measurements and Modeling of Carbon Nanotube Array Growth Kinetics during Chemical Vapor Deposition. *Appl. Phys. A: Mater. Sci. Process.* **2005**, *81*, 223–240.
24. Hart, A. J.; van Laake, L.; Slocum, A. H. Desktop Growth of Carbon-Nanotube Monoliths with *In Situ* Optical Imaging. *Small* **2007**, *3*, 772–777.
25. Meshot, E. R.; Hart, A. J. Abrupt Self-Termination of Vertically Aligned Carbon Nanotube Growth. *Appl. Phys. Lett.* **2008**, *92*, 113107.
26. Einarsson, E.; Murakami, Y.; Kadowaki, M.; Maruyama, S. Growth Dynamics of Vertically Aligned Single-Walled Carbon Nanotubes from *In Situ* Measurements. *Carbon* **2008**, *46*, 923–930.
27. Puretzky, A. A.; Eres, G.; Rouleau, C. M.; Ivanov, I. N.; Geohegan, D. B. Real-Time Imaging of Vertically Aligned Carbon Nanotube Array Growth Kinetics. *Nanotechnology* **2008**, *19*, 055605.
28. Meshot, E. R.; Plata, D. L.; Tawfick, S.; Zhang, Y. Y.; Verploegen, E. A.; Hart, A. J. Engineering Vertically Aligned Carbon Nanotube Growth by Decoupled Thermal Treatment of Precursor and Catalyst. *ACS Nano* **2009**, *3*, 2477–2486.
29. Futaba, D. N.; Hata, K.; Yamada, T.; Mizuno, K.; Yumura, M.; Iijima, S. Kinetics of Water-Assisted Single-Walled Carbon Nanotube Synthesis Revealed by a Time-Evolution Analysis. *Phys. Rev. Lett.* **2005**, *95*, 056104.
30. Zhu, L. B.; Hess, D. W.; Wong, C. P. Monitoring Carbon Nanotube Growth by Formation of Nanotube Stacks and Investigation of the Diffusion-Controlled Kinetics. *J. Phys. Chem. B* **2006**, *110*, 5445–5449.
31. Patole, S. P.; Park, J. H.; Lee, T. Y.; Lee, J. H.; Patole, A. S.; Yoo, J. B. Growth Interruption Studies on Vertically Aligned 2−3 Wall Carbon Nanotubes by Water Assisted Chemical Vapor Deposition. *Appl. Phys. Lett.* **2008**, *93*, 114101–114104.
32. Stadermann, M.; Sherlock, S. P.; In, J.-B.; Fornasiero, F.; Park, H. G.; Artyukhin, A. B.; Wang, Y.; De Yoreo, J. J.; Grigoropoulos, C. P.; Bakajin, O.; *et al.* Mechanism and Kinetics of Growth Termination in Controlled Chemical Vapor Deposition Growth of Multiwall Carbon Nanotube Arrays. *Nano Lett.* **2009**, *9*, 738–744.
33. Shanov, V.; Mallik, N.; Chu, W.; Li, W.; Jayasinghe, C.; Yun, Y.; Schulz, M. J.; Yarmolenko, S.; Salunke, P.; Li, G. Advances in Synthesis and Application of Carbon Nanotube Materials. Materials Science and Technology Conference, Pittsburgh, Pennsylvania, **2008**.
34. Mattevi, C.; Wirth, C. T.; Hofmann, S.; Blume, R.; Cantoro, M.; Ducati, C.; Cepek, C.; Knop-Gericke, A.; Milne, S.; Castellarin-Cudia, C.; *et al. In-Situ* X-ray Photoelectron Spectroscopy Study of Catalyst−Support Interactions and Growth of Carbon Nanotube Forests. *J. Phys. Chem. C* **2008**, *112*, 12207–12213.
35. Patole, S. P.; Alegaonkar, P. S.; Lee, H. C.; Yoo, J. B. Optimization of Water Assisted Chemical Vapor Deposition Parameters for Super Growth of Carbon Nanotubes. *Carbon* **2008**, *46*, 1987–1993.
36. Wu, J.; Huang, Q. W.; Ma, Y. F.; Huang, Y.; Liu, Z. F.; Yang, X. Y.; Chen, Y. S.; Chen, D. P. Distortion of Carbon Nanotube Array and Its Influence on Carbon Nanotube Growth and Termination. *Colloids Surf., A* **2008**, *313*, 13–17.
37. Dell'Acqua-Bellavitis, L.; Ballard, J.; Ajayan, P.; Siegel, R. Kinetics for the Synthesis Reaction of Aligned Carbon Nanotubes: A Study Based on *In Situ* Diffractography. *Nano Lett.* **2004**, *4*, 1613–1620.
38. Iwasaki, T.; Zhong, G. F.; Aikawa, T.; Yoshida, T.; Kawarada, H. Direct Evidence for Root Growth of Vertically Aligned Single-Walled Carbon Nanotubes by Microwave Plasma Chemical Vapor Deposition. *J. Phys. Chem. B* **2005**, *109*, 19556–19559.
39. Valiente, A. M.; Lopez, P. N.; Ramos, I. R.; Ruiz, A. G.; Li, C.; Xin, Q. *In Situ* Study of Carbon Nanotube Formation by C_2H_2 Decomposition on an Iron-Based Catalyst. *Carbon* **2000**, *38*, 2003–2006.

40. Yasuda, S.; Hiraoka, T.; Futaba, D. N.; Yamada, T.; Yumura, M.; Hata, K. Existence and Kinetics of Graphitic Carbonaceous Impurities in Carbon Nanotube Forests To Assess the Absolute Purity. *Nano Lett.* **2009**, *9*, 769–773.
41. Jackson, J. J.; Puretzky, A. A.; More, K. L.; Rouleau, C. M.; Eres, G.; Geohegan, D. B. Pulsed Growth of Vertically Aligned Nanotube Arrays with Variable Density. *ACS Nano* **2010**, *4*, 7573–7581.
42. Picher, M.; Anglaret, E.; Arenal, R.; Jourdain, V. Self-Deactivation of Single-Walled Carbon Nanotube Growth Studied by *In Situ* Raman Measurements. *Nano Lett.* **2009**, *9*, 542–547.
43. Chiashi, S.; Kohno, M.; Takata, Y.; Maruyama, S. Localized Synthesis of Single-Walled Carbon Nanotubes on Silicon Substrates by a Laser Heating Catalytic CVD; Cola'05: 8th International Conference on Laser Ablation. *J. Phys. Conf. Ser.*; Hess, W. P., Herman, P. R., Bauerle, D., Koinuma, H., Eds.; 2007; Vol. 59, pp 155–158.
44. Li-Pook-Than, A.; Lefebvre, J.; Finnie, P. Phases of Carbon Nanotube Growth and Population Evolution from *In Situ* Raman Spectroscopy during Chemical Vapor Deposition. *J. Phys. Chem. C* **2010**, *114*, 11018–11025.
45. Latorre, N.; Romeo, E.; Cazana, F.; Ubieto, T.; Royo, C.; Villacampa, J. J.; Monzon, A. Carbon Nanotube Growth by Catalytic Chemical Vapor Deposition: A Phenomenological Kinetic Model. *J. Phys. Chem. C* **2010**, *114*, 4773–4782.
46. Dresselhaus, M. S.; Dresselhaus, G.; Saito, R.; Jorio, A. Raman Spectroscopy of Carbon Nanotubes. *Phys. Rep.-Rev. Sec. Phys. Lett.* **2005**, *409*, 47–99.
47. Kim, Y. A.; Kakegawa, H.; Fujisawa, K.; Shimamoto, D.; Muramatsu, H.; Kim, J. H.; Jung, Y. C.; Hayashi, T.; Endo, M.; Terrones, M.; Dresselhaus, M. S. Sensitive G-Band Raman Features for the Electrical Conductivity of Multi-Walled Carbon Nanotubes. *J. Nanosci. Nanotechnol.* **2010**, *10*, 3940–3944.
48. Wang, B. N.; Bennett, R. D.; Verploegen, E.; Hart, A. J.; Cohen, R. E. Characterizing the Morphologies of Mechanically Manipulated Multiwall Carbon Nanotube Films by Small-Angle X-ray Scattering. *J. Phys. Chem. C* **2007**, *111*, 17933–17940.
49. Wang, B. N.; Bennett, R. D.; Verploegen, E.; Hart, A. J.; Cohen, R. E. Quantitative Characterization of the Morphology of Multiwall Carbon Nanotube Films by Small-Angle X-ray Scattering. *J. Phys. Chem. C* **2007**, *111*, 5859–5865.
50. Verploegen, E.; Hart, A. J.; De Volder, M.; Tawfick, S.; Chia, K.-K.; Cohen, R. E. Non-destructive Characterization of Structural Hierarchy within Aligned Carbon Nanotube Assemblies. *J. Appl. Phys.* **2011**, *109*, 094316-5.
51. Louchev, O. A.; Laude, T.; Sato, Y.; Kanda, H. Diffusion-Controlled Kinetics of Carbon Nanotube Forest Growth by Chemical Vapor Deposition. *J. Chem. Phys.* **2003**, *118*, 7622–7634.
52. Wood, R. F.; Pannala, S.; Wells, J. C.; Puretzky, A. A.; Geohegan, D. B. Simple Model of the Interrelation between Single- and Multiwall Carbon Nanotube Growth Rates for the CVD Process. *Phys. Rev. B* **2007**, *75*, 235446–235454.
53. Hubbell, J. H. Compilation of Photon Cross-Sections: Some Historical Remarks and Current Status. *X-Ray Spectrom.* **1999**, *28*, 215–223.
54. Hubbell, J. H. Review and History of Photon Cross Section Calculations. *Phys. Med. Biol.* **2006**, *51*, R245–R262.
55. Arcos, T. D. L.; Oelhafen, P.; Thommen, V.; Mathys, D. The Influence of Catalyst's Oxidation Degree on Carbon Nanotube Growth as a Substrate-Independent Parameter. *J. Phys. Chem. C* **2007**, *111*, 16392–16396.
56. Okita, A.; Ozeki, A.; Suda, Y.; Nakamura, J.; Oda, A.; Bhattacharyya, K.; Sugawara, H.; Sakai, Y. Analysis of Oxidation State of Multilayered Catalyst Thin Films for Carbon Nanotube Growth Using Plasma-Enhanced Chemical Vapor Deposition. *Jpn. J. Appl. Phys., Part 1* **2006**, *45*, 8323–8329.
57. Picher, M.; Anglaret, E.; Arenal, R.; Jourdain, V. Processes Controlling the Diameter Distribution of Single-Walled Carbon Nanotubes during Catalytic Chemical Vapor Deposition. *ACS Nano* **2011**, *5*, 2118–2125.
58. Wang, H.; Xu, Z.; Eres, G. Order in Vertically Aligned Carbon Nanotube Arrays. *Appl. Phys. Lett.* **2006**, *88*, 213111–213114.
59. Unpublished data.
60. Hofmann, S.; Sharma, R.; Ducati, C.; Du, G.; Mattevi, C.; Cepek, C.; Cantoro, M.; Pisana, S.; Parvez, A.; Cervantes-Sodi, F.; *et al. In Situ* Observations of Catalyst Dynamics During Surface-Bound Carbon Nanotube Nucleation. *Nano Lett.* **2007**, *7*, 602–608.
61. Hermans, P. H. *Contribution to the Physics of Cellulose Fibres; A Study in Sorption, Density, Refractive Power and Orientation*; Elsevier: Amsterdam, 1946.
62. Lin, M.; Tan, J. P. Y.; Boothroyd, C.; Loh, K. P.; Tok, E. S.; Foo, Y. L. Direct Observation of Single-Walled Carbon Nanotube Growth at the Atomistic Scale. *Nano Lett.* **2006**, *6*, 449–452.
63. Yasuda, S.; Futaba, D. N.; Yamada, T.; Satou, J.; Shibuya, A.; Takai, H.; Arakawa, K.; Yumura, M.; Hata, K. Improved and Large Area Single-Walled Carbon Nanotube Forest Growth by Controlling the Gas Flow Direction. *ACS Nano* **2009**, *3*, 4164–4170.
64. Vinten, P.; Lefebvre, J.; Finnie, P. Kinetic Critical Temperature and Optimized Chemical Vapor Deposition Growth of Carbon Nanotubes. *Chem. Phys. Lett.* **2009**, *469*, 293–297.
65. Lacava, A. I.; Bernardo, C. A.; Trimm, D. L. Studies of Deactivation of Metals by Carbon Deposition. *Carbon* **1982**, *20*, 219–223.
66. Richards, F. J. A Flexible Growth Function for Empirical Use. *J. Exp. Bot.* **1959**, *10*, 290–300.
67. Winsor, C. P. The Gompertz Curve as a Growth Curve. *Proc. Natl. Acad. Sci. U.S.A.* **1932**, *18*, 1–8.
68. Laird, A. K. Dynamics of Tumor Growth. *Br. J. Cancer* **1964**, *18*, 490.
69. Zwietering, M. H.; Jongenburger, I.; Rombouts, F. M.; Vantriet, K. Modeling of the Bacterial-Growth Curve. *Appl. Environ. Microbiol.* **1990**, *56*, 1875–1881.
70. Necula, M.; Kuret, J.; Static Laser, A Light Scattering Assay for Surfactant-Induced Tau Fibrillization. *Anal. Biochem.* **2004**, *333*, 205–215.
71. Xiang, R.; Yang, Z.; Zhang, Q.; Luo, G.; Qian, W.; Wei, F.; Kadowaki, M.; Einarsson, E.; Maruyama, S. Growth Deceleration of Vertically Aligned Carbon Nanotube Arrays: Catalyst Deactivation or Feedstock Diffusion Controlled? *J Phys. Chem. C* **2008**, *112*, 4892–4896.
72. Zhu, L. B.; Xu, J. W.; Xiao, F.; Jiang, H. J.; Hess, D. W.; Wong, C. P. The Growth of Carbon Nanotube Stacks in the Kinetics-Controlled Regime. *Carbon* **2007**, *45*, 344–348.
73. Zhang, G. Y.; Mann, D.; Zhang, L.; Javey, A.; Li, Y. M.; Yenilmez, E.; Wang, Q.; McVittie, J. P.; Nishi, Y.; Gibbons, J.; *et al.* Ultra-High-Yield Growth of Vertical Single-Walled Carbon Nanotubes: Hidden Roles of Hydrogen and Oxygen. *Proc. Natl. Acad. Sci. U.S.A.* **2005**, *102*, 16141–16145.
74. Hata, K.; Futaba, D. N.; Mizuno, K.; Namai, T.; Yumura, M.; Iijima, S. Water-Assisted Highly Efficient Synthesis of Impurity-Free Single-Waited Carbon Nanotubes. *Science* **2004**, *306*, 1362–1364.
75. Magrez, A.; Seo, J. W.; Kuznetsov, V. L.; Forro, L. Evidence of an Equimolar C_2H_2-CO_2 Reaction in the Synthesis of Carbon Nanotubes. *Angew. Chem., Int. Ed.* **2007**, *46*, 441–444.
76. Nasibulin, A. G.; Brown, D. P.; Queipo, P.; Gonzalez, D.; Jiang, H.; Kauppinen, E. I. An Essential Role of CO_2 and H_2O during Single-Walled CNT Synthesis from Carbon Monoxide. *Chem. Phys. Lett.* **2006**, *417*, 179–184.
77. Futaba, D. N.; Hata, K.; Namai, T.; Yamada, T.; Mizuno, K.; Hayamizu, Y.; Yumura, M.; Iijima, S. 84% Catalyst Activity of Water-Assisted Growth of Single Walled Carbon Nanotube Forest Characterization by a Statistical and Macroscopic Approach. *J. Phys. Chem. B* **2006**, *110*, 8035–8038.
78. Pint, C. L.; Pheasant, S. T.; Parra-Vasquez, A. N. G.; Horton, C.; Xu, Y. Q.; Hauge, R. H. Investigation of Optimal Parameters for Oxide-Assisted Growth of Vertically Aligned Single-Walled Carbon Nanotubes. *J. Phys. Chem. C* **2009**, *113*, 4125–4133.
79. Nishino, H.; Yasuda, S.; Namai, T.; Futaba, D. N.; Yamada, T.; Yumura, M.; Iijima, S.; Hata, K. Water-Assisted Highly Efficient Synthesis of Single-Walled Carbon Nanotubes Forests from Colloidal Nanoparticle Catalysts. *J. Phys. Chem. C* **2007**, *111*, 17961–17965.

80. Zhang, Y. Y.; Gregoire, J. M.; van Dover, R. B.; Hart, A. J. Ethanol-Promoted High-Yield Growth of Few-Walled Carbon Nanotubes. *J. Phys. Chem. C* **2010**, *114*, 6389–6395.
81. Frenklach, M.; Clary, D. Aspects of Autocatalytic Reaction-Kinetics. *Ind. Eng. Chem. Fundam.* **1983**, *22*, 433–436.
82. Eres, G.; Rouleau, C. M.; Yoon, M.; Puretzky, A. A.; Jackson, J. J.; Geohegan, D. B. Model for Self-Assembly of Carbon Nanotubes from Acetylene Based on Real-Time Studies of Vertically Aligned Growth Kinetics. *J. Phys. Chem. C* **2009**, *113*, 15484–15491.
83. Plata, D. e. L.; Meshot, E. R.; Reddy, C. M.; Hart, A. J.; Gschwend, P. M. Multiple Alkynes React with Ethylene To Enhance Carbon Nanotube Synthesis, Suggesting a Polymerization-like Formation Mechanism. *ACS Nano* **2010**, *4*, 7185–7192.
84. Plata, D. e. L.; Hart, A. J.; Reddy, C. M.; Gschwend, P. M. Early Evaluation of Potential Environmental Impacts of Carbon Nanotube Synthesis by Chemical Vapor Deposition. *Environ. Sci. Technol.* **2009**, *43*, 8367–8373.
85. Liu, K.; Liu, P.; Jiang, K.; Fan, S. S. Effect of Carbon Deposits on the Reactor Wall during the Growth of Multi-Walled Carbon Nanotube Arrays. *Carbon* **2007**, *45*, 2379–2387.
86. Monzon, A.; Lolli, G.; Cosma, S.; Mohamed, S. B.; Resasco, D. E. Kinetic Modeling of the SWNT Growth by CO Disproportionation on CoMo Catalysts. *J. Nanosci. Nanotechnol.* **2008**, *8*, 6141–6152.
87. Meshot, E. R.; Bedewy, M.; Hart, A. J. Rapid Dynamics of Catalyst Particle Formation and Carbon Nanotube Growth Revealed by High-Speed *In Situ* X-ray Scattering. Manuscript in preparation.
88. Sushumna, I.; Ruckenstein, E. Role of Physical and Chemical Interactions in the Behavior of Supported Metal-Catalysts—Iron on Alumina—A Case-Study. *J. Catal.* **1985**, *94*, 239–288.
89. De los Arcos, T.; Vonau, F.; Garnier, M. G.; Thommen, V.; Boyen, H. G.; Oelhafen, P.; Duggelin, M.; Mathis, D.; Guggenheim, R. Influence of Iron−Silicon Interaction on the Growth of Carbon Nanotubes Produced by Chemical Vapor Deposition. *Appl. Phys. Lett.* **2002**, *80*, 2383–2385.
90. Paparazzo, E. XPS Analysis of Iron Aluminum-Oxide Systems. *Appl. Surf. Sci.* **1986**, *25*, 1–12.
91. Byrd, J. E.; Perona, M. J. Kinetics of Popping of Popcorn. *Cereal Chem.* **2005**, *82*, 53–59.
92. Kim, D. H.; Lipke, E. A.; Kim, P.; Cheong, R.; Thompson, S.; Delannoy, M.; Suh, K. Y.; Tung, L.; Levchenko, A. Nanoscale Cues Regulate the Structure and Function of Macroscopic Cardiac Tissue Constructs. *Proc. Natl. Acad. Sci. U.S.A.* **2010**, *107*, 565–570.
93. Kukovitsky, E. F.; L'Vov, S. G.; Sainov, N. A.; Shustov, V. A.; Chernozatonskii, L. A. Correlation between Metal Catalyst Particle Size and Carbon Nanotube Growth. *Chem. Phys. Lett.* **2002**, *355*, 497–503.
94. Nerushev, O. A.; Dittmar, S.; Morjan, R. E.; Rohmund, F.; Campbell, E. E. B. Particle Size Dependence and Model for Iron-Catalyzed Growth of Carbon Nanotubes by Thermal Chemical Vapor Deposition. *J. Appl. Phys.* **2003**, *93*, 4185–4190.
95. Helveg, S.; Lopez-Cartes, C.; Sehested, J.; Hansen, P. L.; Clausen, B. S.; Rostrup-Nielsen, J. R.; Abild-Pedersen, F.; Norskov, J. K. Atomic-Scale Imaging of Carbon Nanofibre Growth. *Nature* **2004**, *427*, 426–429.
96. Pint, C. L.; Xu, Y. Q.; Moghazy, S.; Cherukuri, T.; Alvarez, N. T.; Haroz, E. H.; Mahzooni, S.; Doorn, S. K.; Kono, J.; Pasquali, M.; *et al.* Dry Contact Transfer Printing of Aligned Carbon Nanotube Patterns and Characterization of Their Optical Properties for Diameter Distribution and Alignment. *ACS Nano* **2010**, *4*, 1131–1145.
97. Reymann, A. C.; Martiel, J. L.; Cambier, T.; Blanchoin, L.; Boujemaa-Paterski, R.; Thery, M. Nucleation Geometry Governs Ordered Actin Networks Structures. *Nat. Mater.* **2010**, *9*, 827–832.
98. Hubbell, J. H.; Seltzer, S. M. Tables of X-ray Mass Attenuation Coefficients and Mass Energy-Absorption Coefficients from 1 keV to 20 MeV for Elements Z = 1 to 92 and 48 Additional Substances of Dosimetric Interest. *NIST Standard Reference Database 126*, 2004.
99. Horcas, I.; Fernandez, R.; Gomez-Rodriguez, J. M.; Colchero, J.; Gomez-Herrero, J.; Baro, A. M. WSXM: A Software for Scanning Probe Microscopy and a Tool for Nanotechnology. *Rev. Sci. Instrum.* **2007**, *78*, 013705.